Supplementary Materials for

Methane emissions decreased in fossil fuel exploitation and sustainedly increased in microbial source sectors during 1990–2020

Chandra, Naveen *et al.*

*Corresponding author. Email: naveennegi@jamstec.go.jp; prabir@jamstec.go.jp

This PDF file includes:

Supplementary Text
Figs. S1 to S20
Tables S1 to S2

Supplementary Text

Corrections in the EDGAR's ONG emissions over Prudhoe Bay for 1970-2010

The EDGARv6 inventory indicates that there was a consistent hotspot with exceptionally high emissions of CH_4 (~4Tg) from 1970 to 2010 (Fig. S2a). However, this hotspot disappeared suddenly after 2010 (Fig. S2b). It is likely that these observations were artifacts, as the Barrow site, which is closer to the hotspot, did not show such a signal. When we used this emission data in the model, the simulations produced significant peaks and noise in CH_4 molar fraction from 1972 to 2010 at the Barrow site (Fig. S3). This suggests that artifacts may be in the emission hotspots over the Prudhoe Bay region. Therefore, we corrected the hotspot emissions for 1970-2010 by replacing the emissions over the Prudhoe Bay region with 2011 values. Additionally, we scaled the updated global total to the original value to maintain the same magnitude. These corrections significantly improved the simulations at the Barrow site, as shown in Fig. S3. It is worth noting that the 4Tg difference in the NH total in the latitudinal gradient plot is not visible in Fig. S2b, due to the scaling of the corrected emission data to the original value.

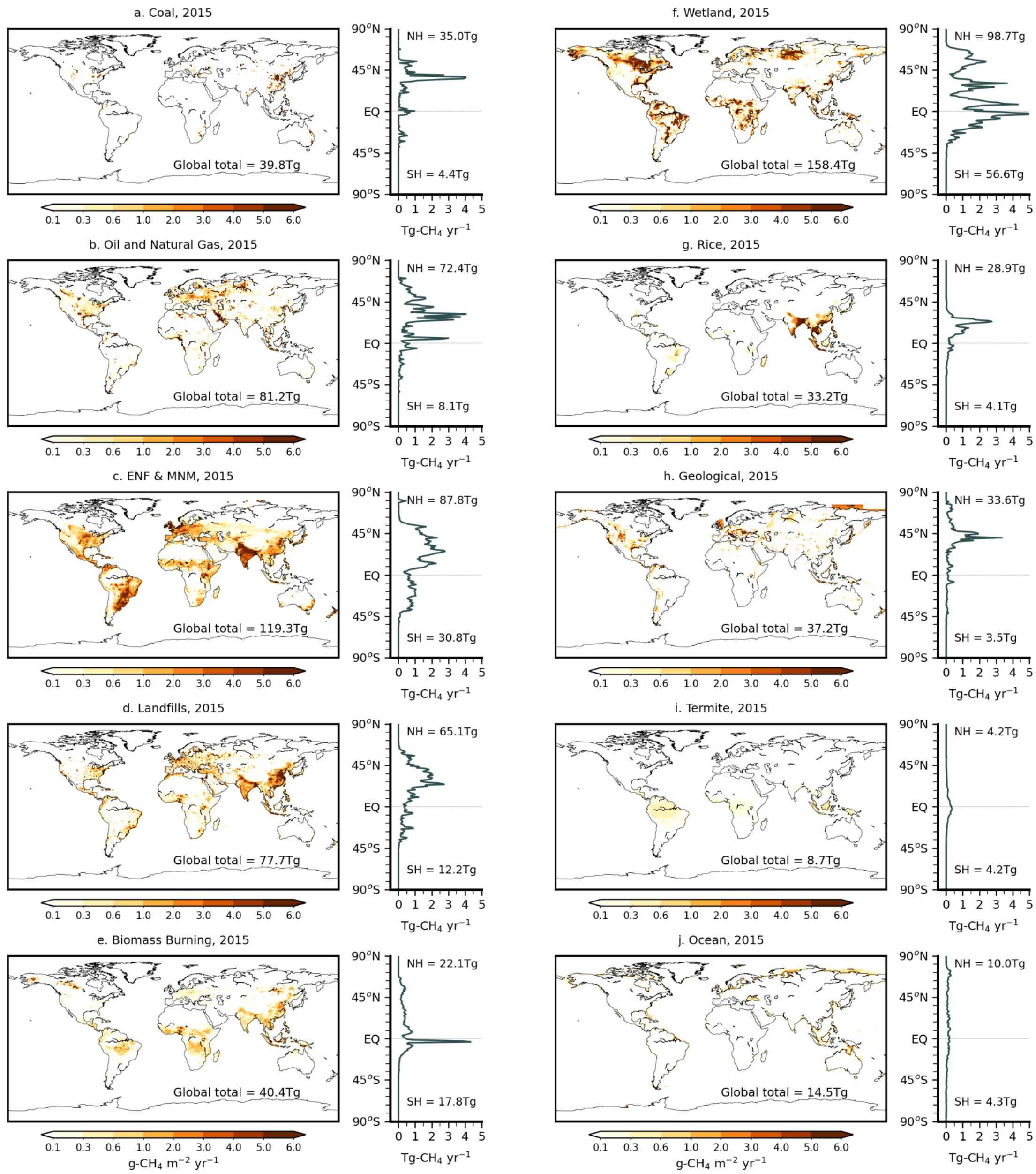

Fig. S1. The global and latitudinal distribution of annual CH_4 emissions from 10 sectors are shown for 2015.

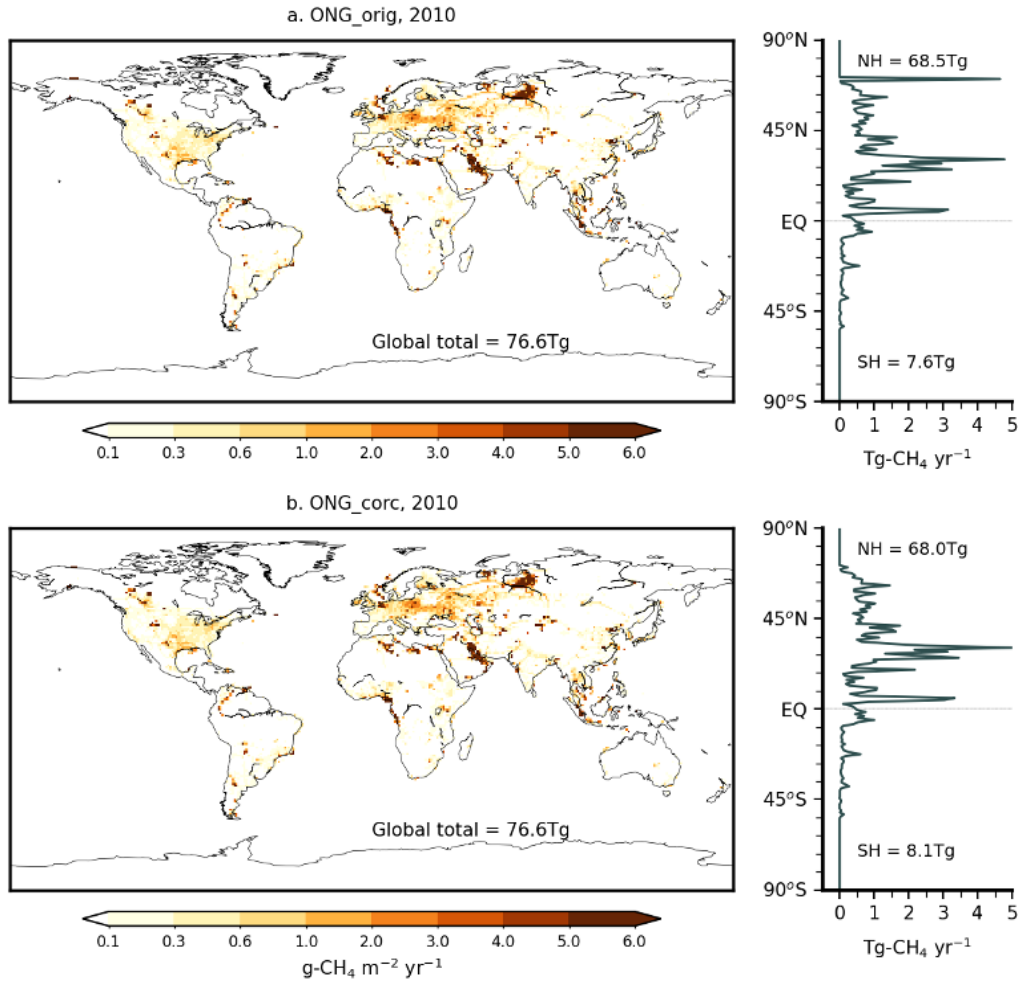

Fig. S2. The spatial and latitudinal distribution of CH_4 emissions from original (a) and corrected (b) ONG source for Prudhoe Bay for 2010. To keep the same global total, the magnitude of corrected ONG emission is scaled to the original one. This is an example; similar features consistently appear from 1970 to 2009.

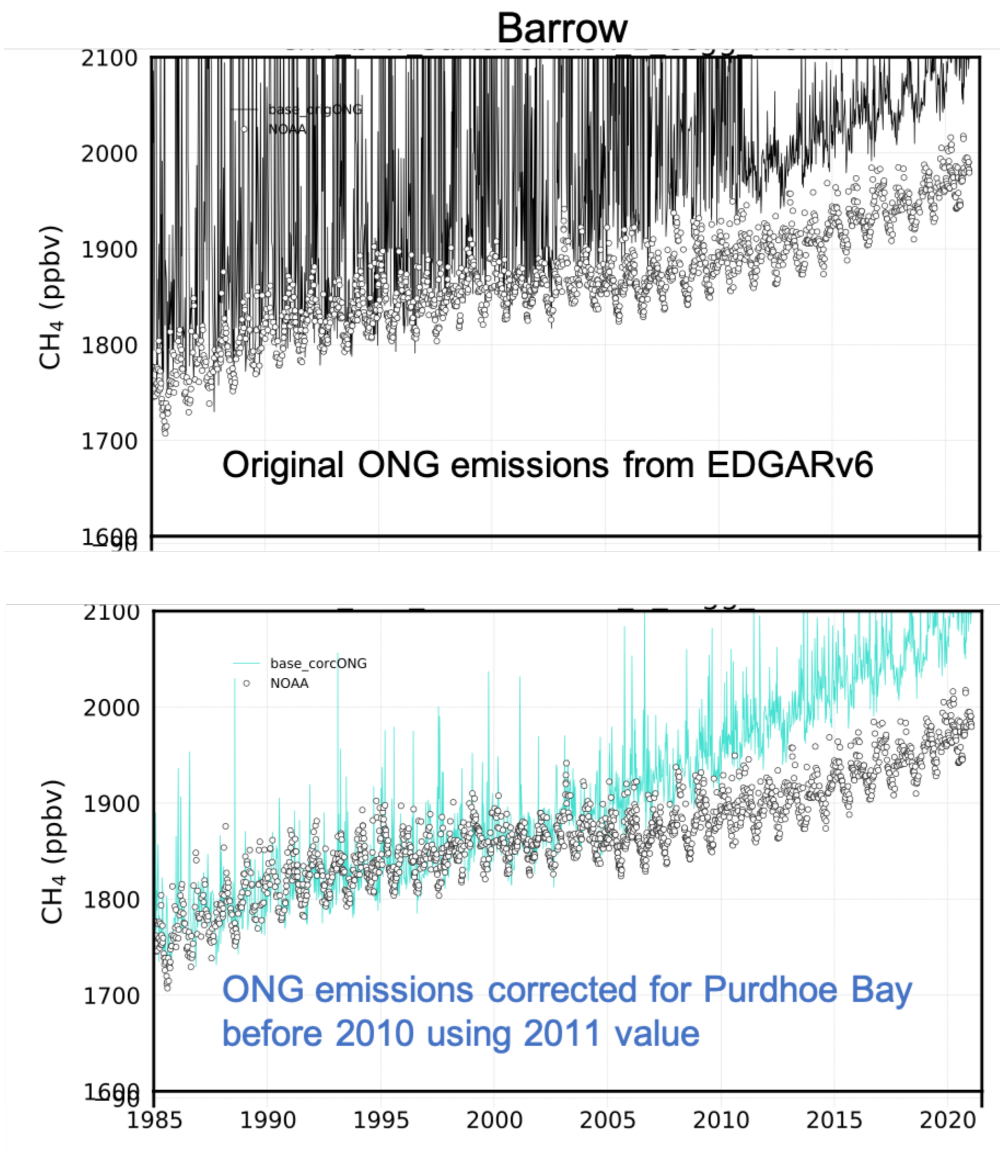

Fig. S3. Validating the correction in ONG emission peaks over Prudhoe Bay before 2011 using measurements over a nearer site, Barrow. The upper panel displays simulations over Barrow, with the peak (shown in Fig. S2a), while the lower panel shows simulations after the correction (shown in Fig. S2b). The high peaks in the upper panel simulations disappeared after the correction in the lower panel, suggesting that they were artifacts.

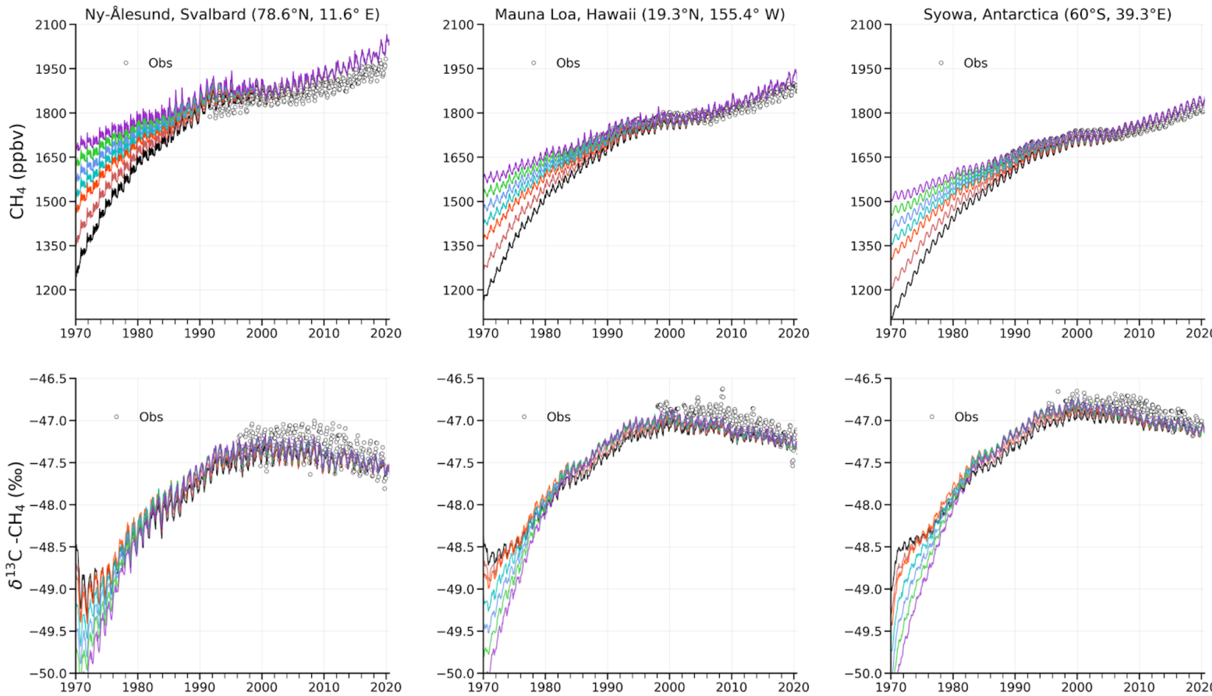

Fig. S4. Sensitivity test for different initial values used for model simulations. Solid lines correspond to simulations using different initial values for CH_4 (range ~1350 ±150 ppb at Syowa station) and $\delta^{13}C$-CH_4 (range -49.5 ±0.7 ‰ at Syowa station). The CH_4 simulations converged to less than a 5% difference from its initial values, while $\delta^{13}C$-CH_4 simulations converged at ~0.02‰ difference, which are small enough to have negligible impact on their long term trend analysis. These sensitivity tests illustrate that the restart values have negligible influence on our analysis results.

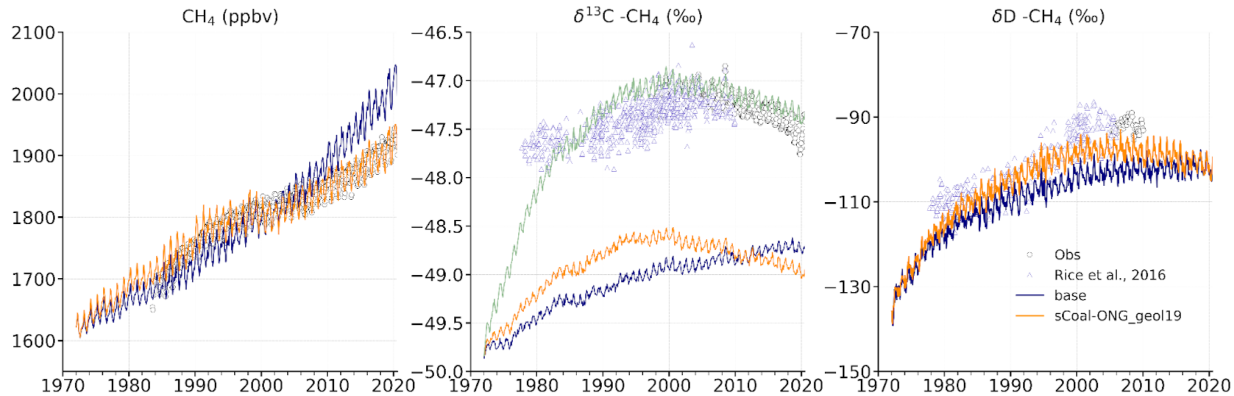

Fig. S5. Modelled CH_4, $\delta^{13}C$-CH_4, and δD-CH_4 over Niwot Ridge, Colorado from different emissions scenarios. The data from Rice et al., [1] (triangles) are also shown to check the evolution of long-term simulations.

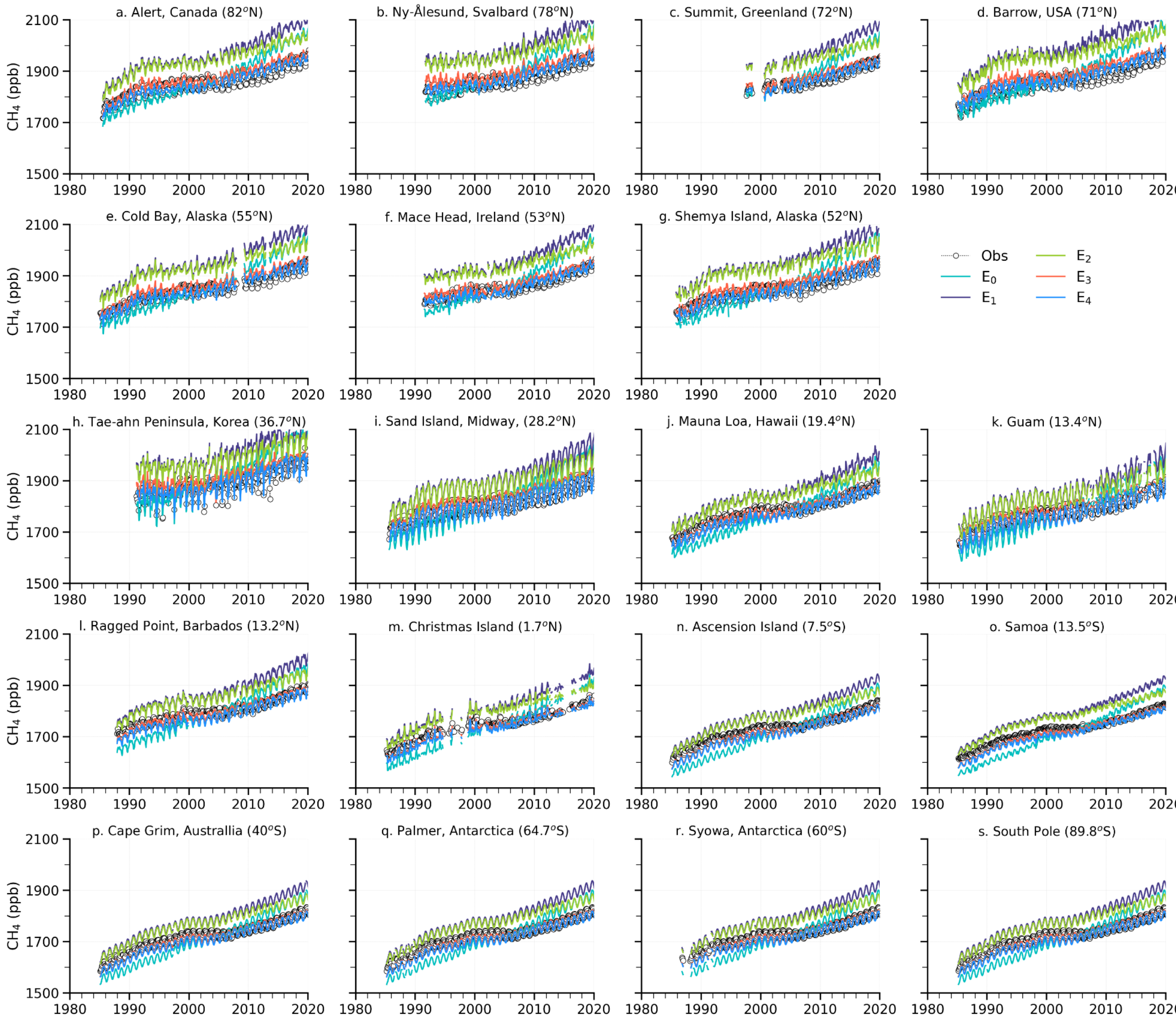

Fig. S6. Comparison of observed and simulated CH_4, based on different scenarios as discussed in Table. 1, over different sites used for calculating sub-hemispheric mean over northern high latitudes (a-g), tropics (h-o), and southern high latitudes (p-s) as shown in Fig. 2.

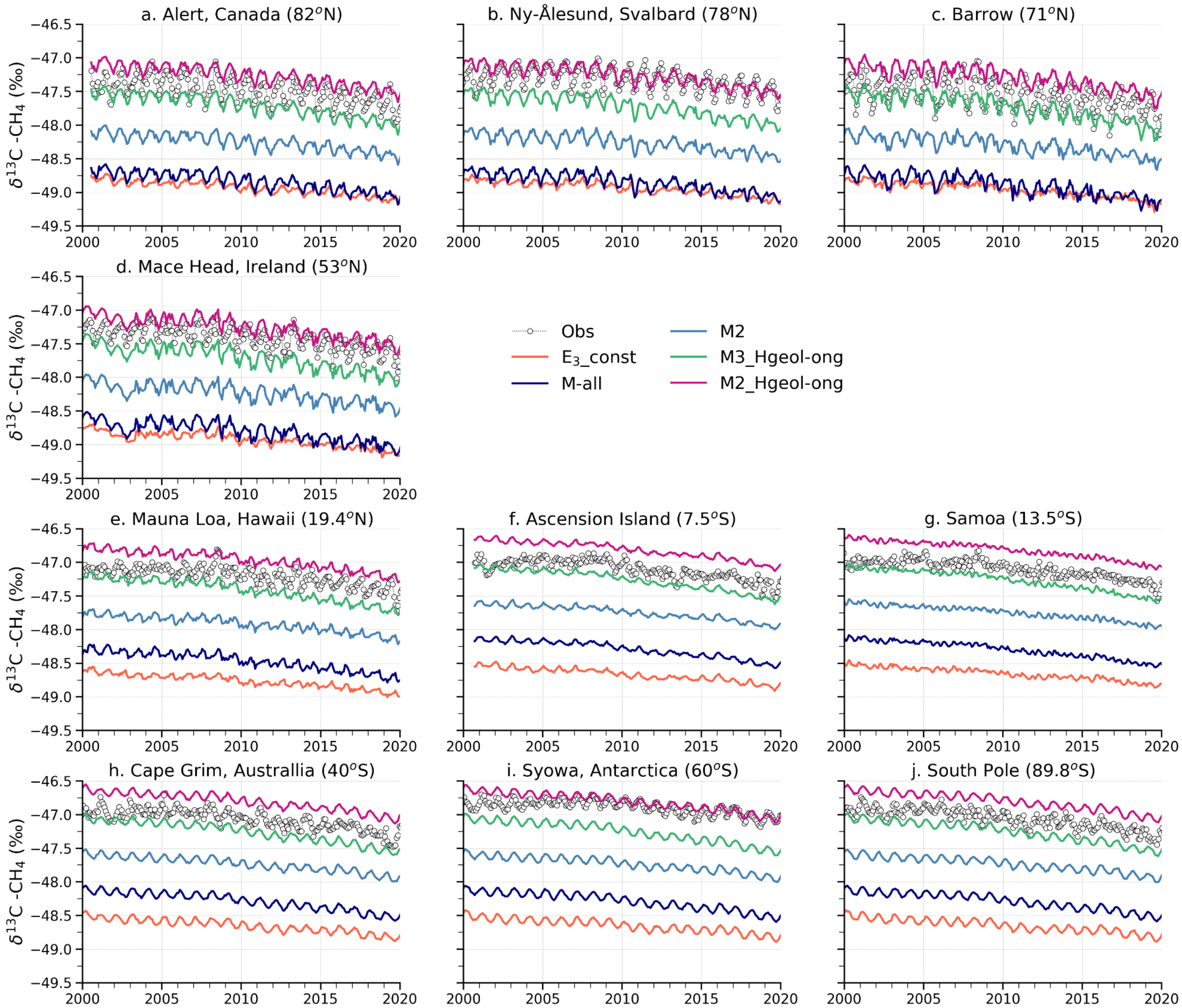

Fig. S7. Modelled (based on $HKIE_{OH}$) and observed $\delta^{13}C$-CH_4 over different sites used for calculating mean over northern high latitudes (a-d), tropics (e-g), and southern high latitudes (h-j).

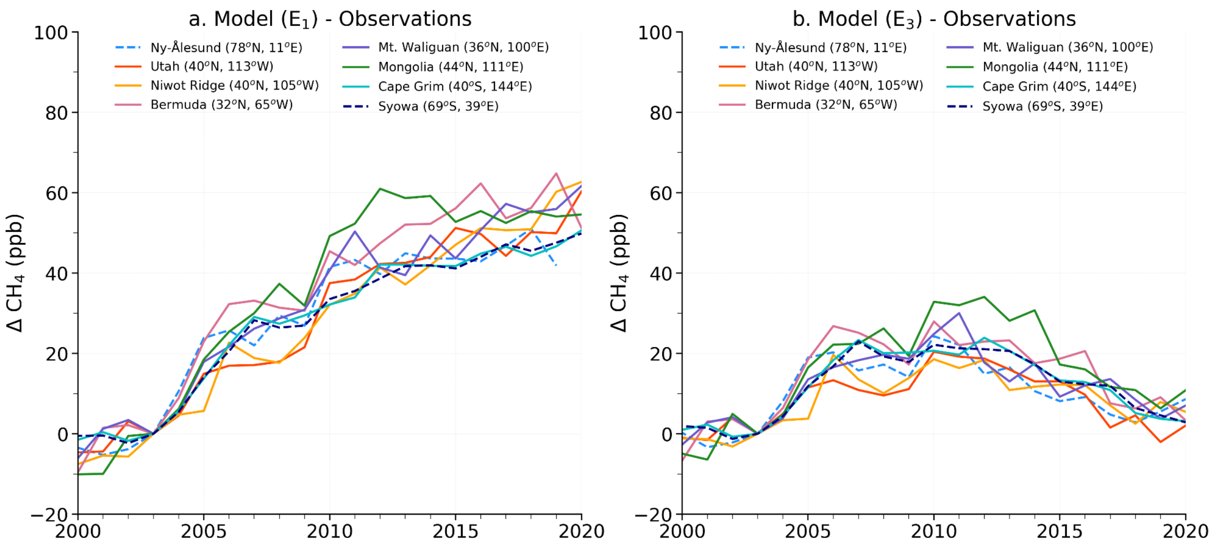

Fig. S8. Difference between observations and simulations based on base (a. E_1) and E_3 (panel "b") emission scenarios over different sites. The differences are adjusted at zero for the value of 2003 to clearly visualize the trend. Removing the unconventional gas emission over the USA and scaling coal emissions over China in a sensitivity E_3 emission scenario help to reduce the model and observations mismatch. The background stations are shown by the dashed lines

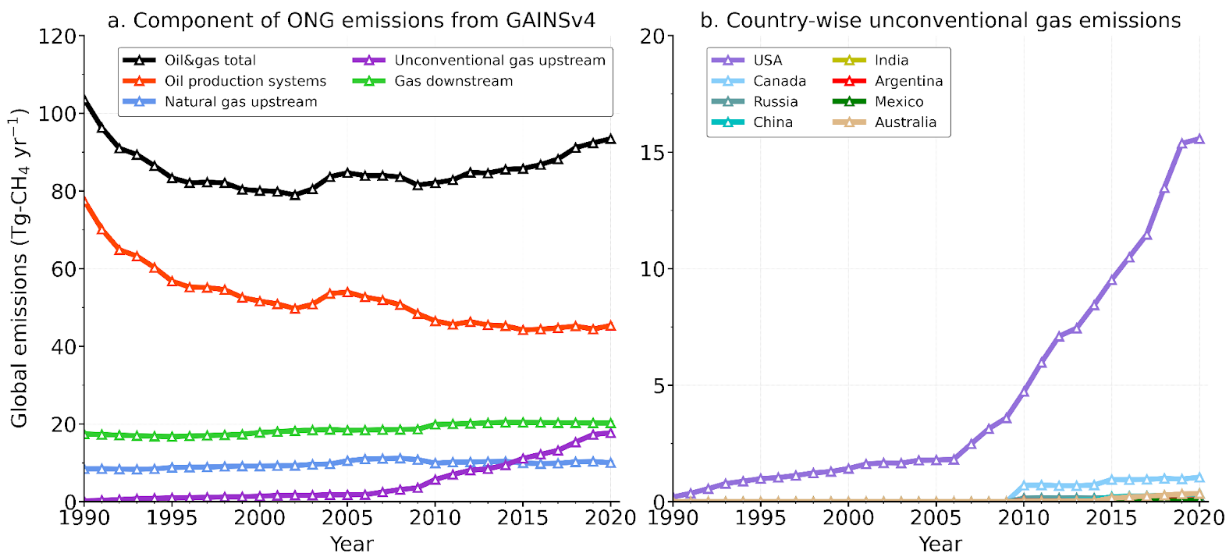

Fig S9. (a). The temporal variability in different sectors contributing to total ONG emissions based on GAINSv4 estimate. (b) Changes of unconventional gas emissions over dominating countries. The mainland USA shares about 90% of total unconventional gas production emissions in the World. There are some also in Canada and China, but otherwise minimal amounts in the rest of the World.

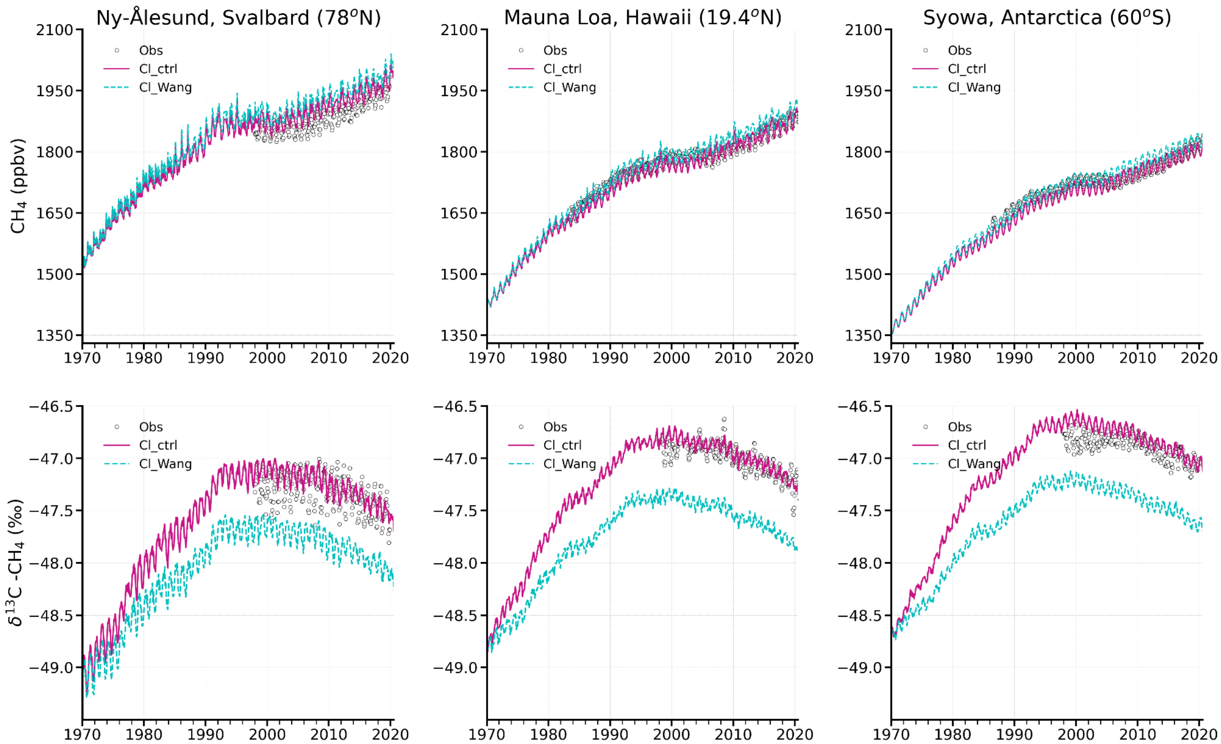

Fig. S10. Comparison between observations and simulations based on control chlorine field (Cl_ctrl; Takigawa et al. [2]) and Wang et al. [3] (Cl_wang) Cl field. Both simulations use the E_3 emission field (Fig. 3 and Table 1) and M2_Hgeol-ong source signature (Fig. 4 and Table 1). The H-KIE_{OH} value (1.0054) is used for δ^{13}C-CH_4 simulations (detail in Fig. 4). Both Cl files show the offset of ~ 0.6‰ in δ^{13}C-CH_4 simulations, but the trends remained unchanged. These sensitivity tests had a relatively low impact on CH_4 simulations.

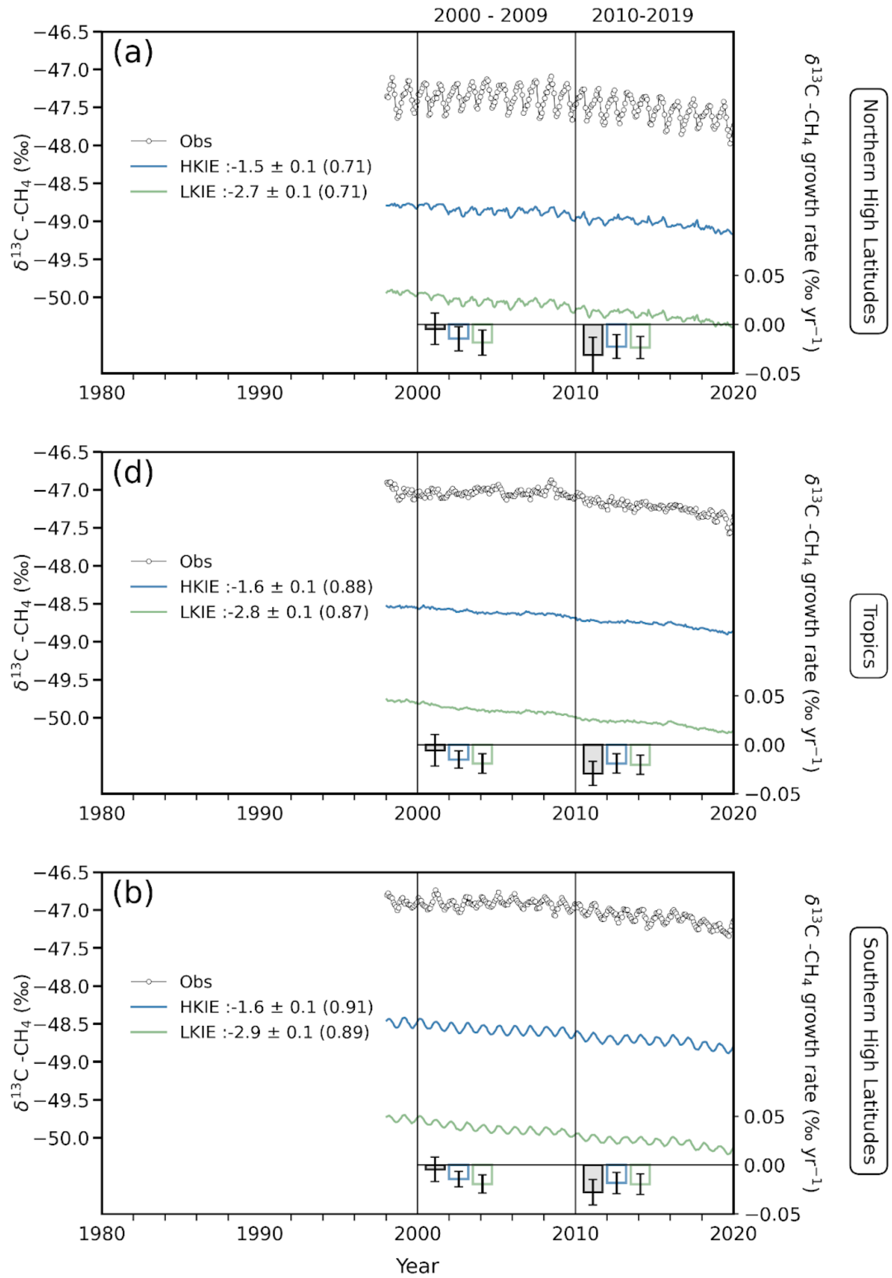

Fig S11. Evaluating the role of KIE_{OH} (for OH) in simulating the atmospheric $\delta^{13}C\text{-}CH_4$ using the base scenario (E_0*), which uses the global invariant signature of $\delta^{13}C$. The KIE_{OH} values are based on Centrel et al. [4] (1.0054: $HKIE_{OH}$) and Saueressig et al. [5] (1.0039: $LKIE_{OH}$). The simulations based on both KIE_{OH} show a difference of 1.2‰, no large difference is observed in the growth rate.

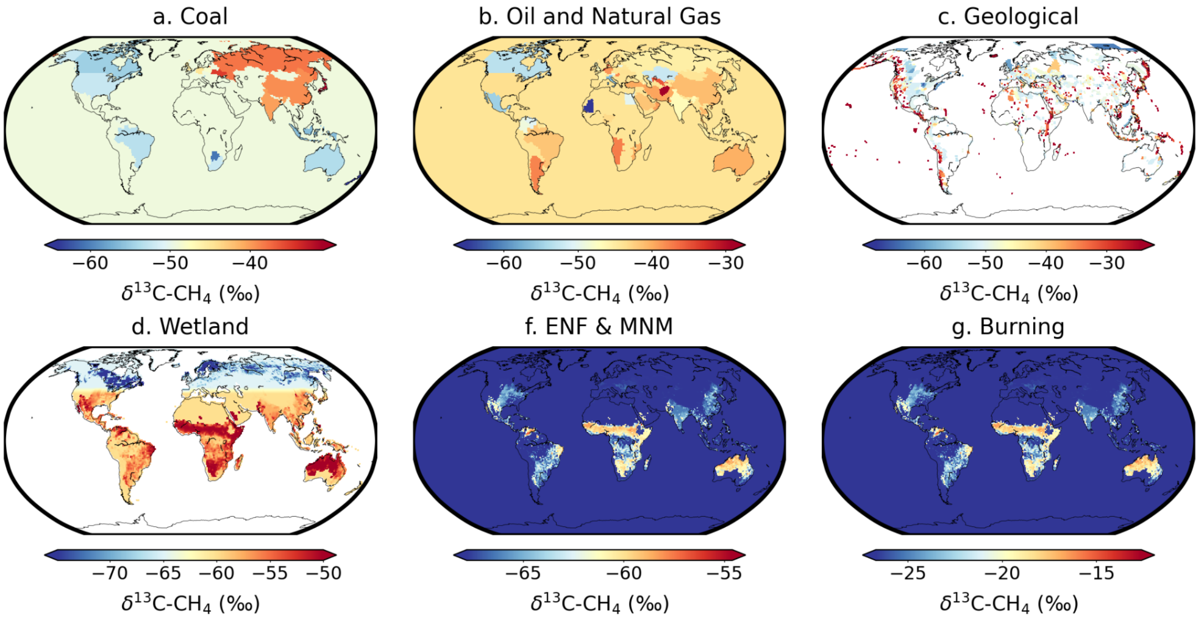

Fig. S12. Source signature maps for six different sectors are used for simulations of $\delta^{13}C$-CH_4. The $\delta^{13}C$ source signatures maps based on the Global $\delta^{13}C$ Source Signature Inventory 2020 for coal, oil and gas (ONG), biomass and biofuel burning, ruminant and wild animal sources [6], spatial maps for wetland sources [7], and geological seeps [8].

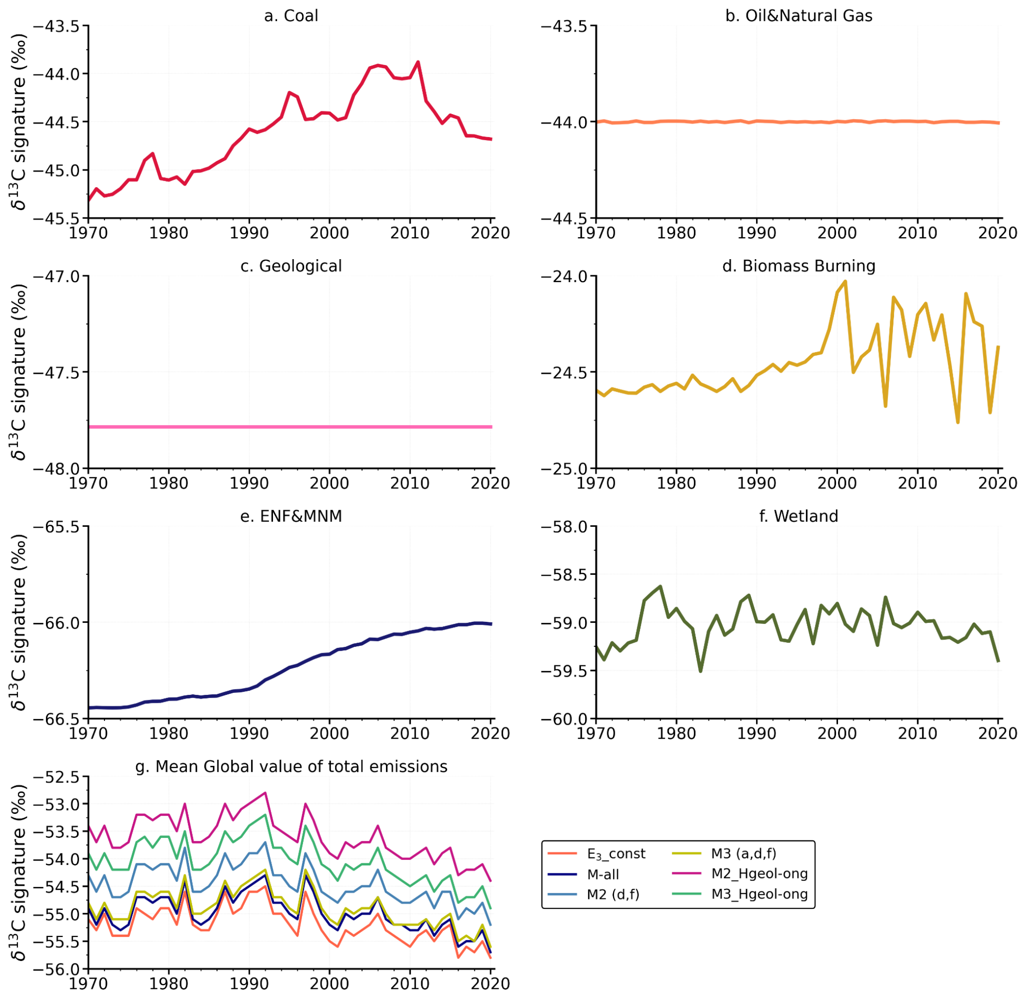

Fig. S13. Emission-weighted global mean source signatures. Trend in global mean source signatures, using geographical isotopic variations (indicated by "Map" in Table 1) weighted by gridded emissions from E_3 scenario, throughout the simulation period. Please note that the global mean signatures using geographical source signatures are different from the global invariant source signature ("E3_const"), used in Fig.2. Time series of the isotopic signature of total CH_4 emissions using different combinations of source signature, as discussed in main Fig. 4, under common emissions E_3, is shown in "g" (Refer to Table 1 for more details).

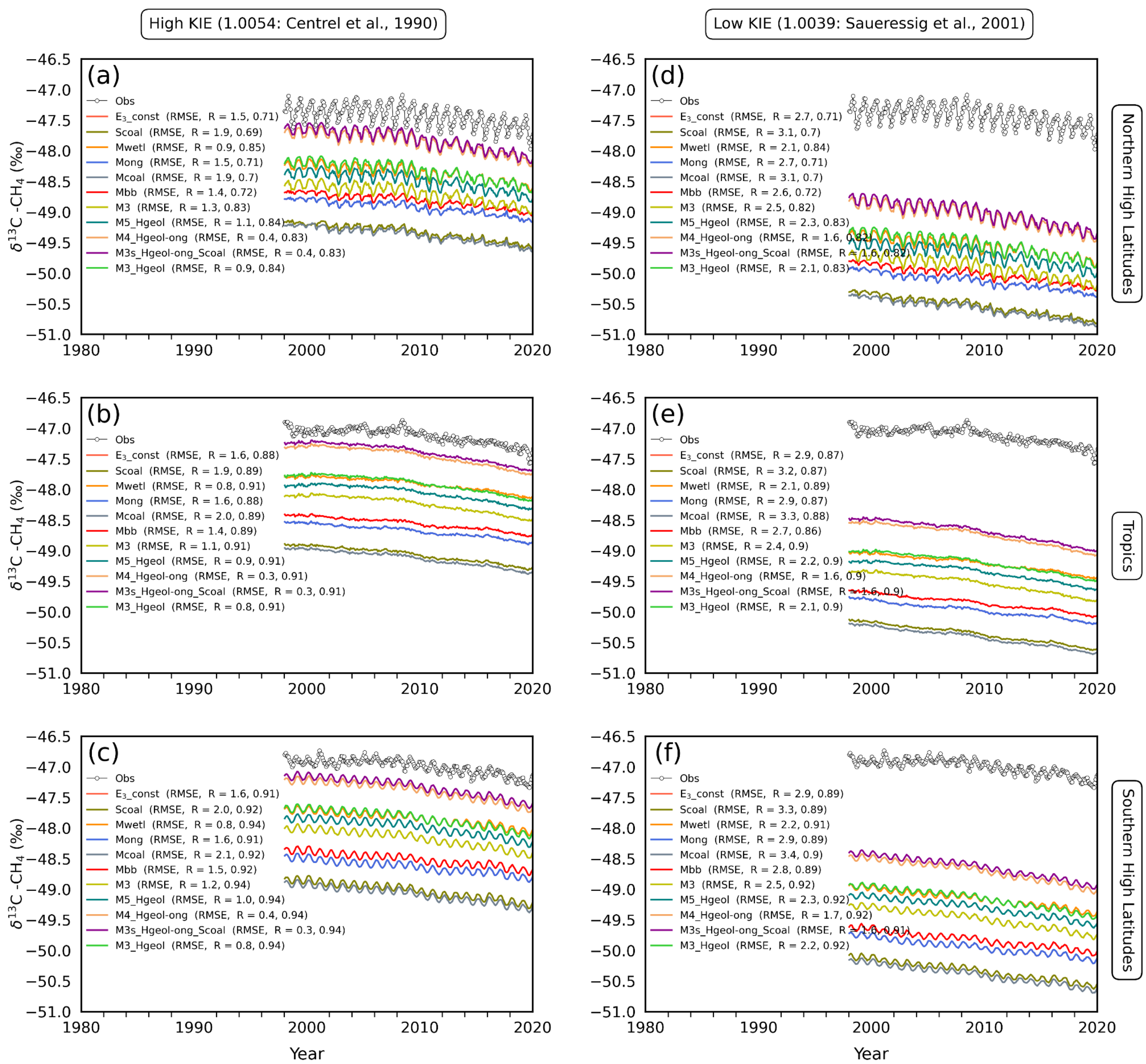

Fig. S14. Same as Fig.4 in the main text, but for remaining sensitivity simulation cases.

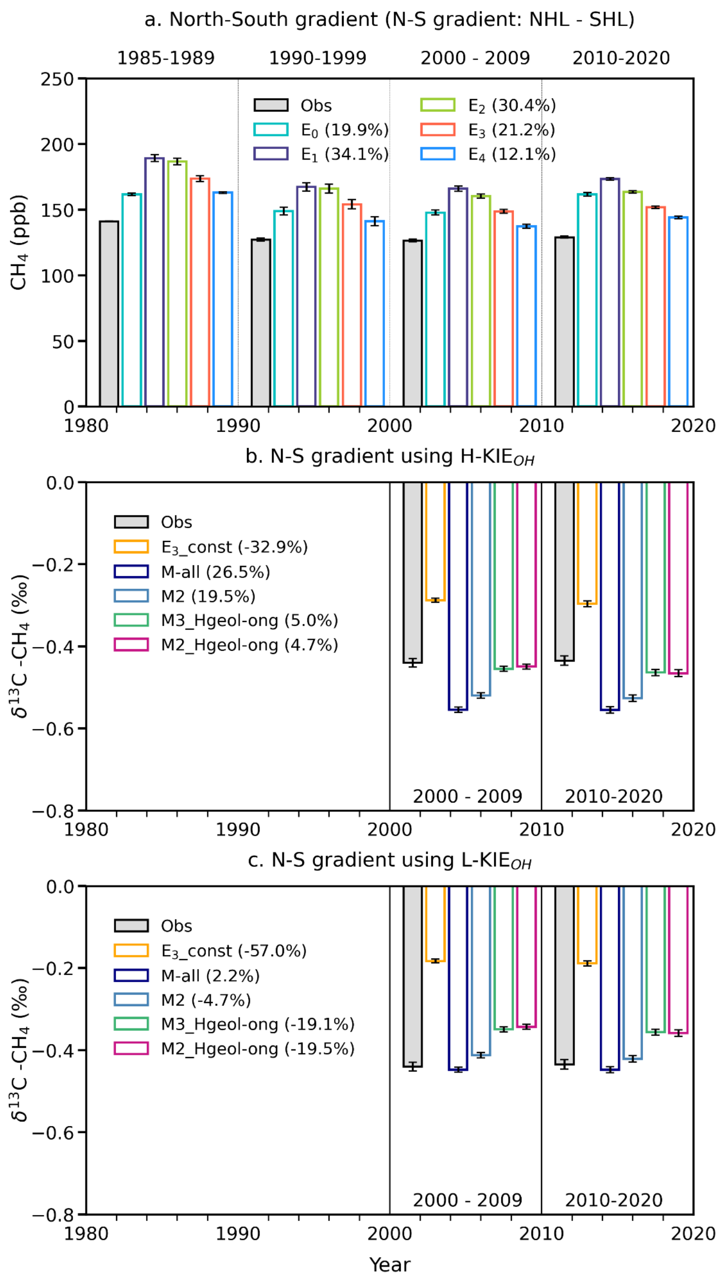

Fig. S15. North-South (N-S) gradient for CH_4 and using different scenarios (Details in Table. 1). The numbers shown in the legends are the percentage differences from the observations. Positive values represent the overestimation, while negative represent the underestimation. The simulations in the "b" and "c" columns are based on E_3 emissions and source signatures, but different KIE_{OH} values.

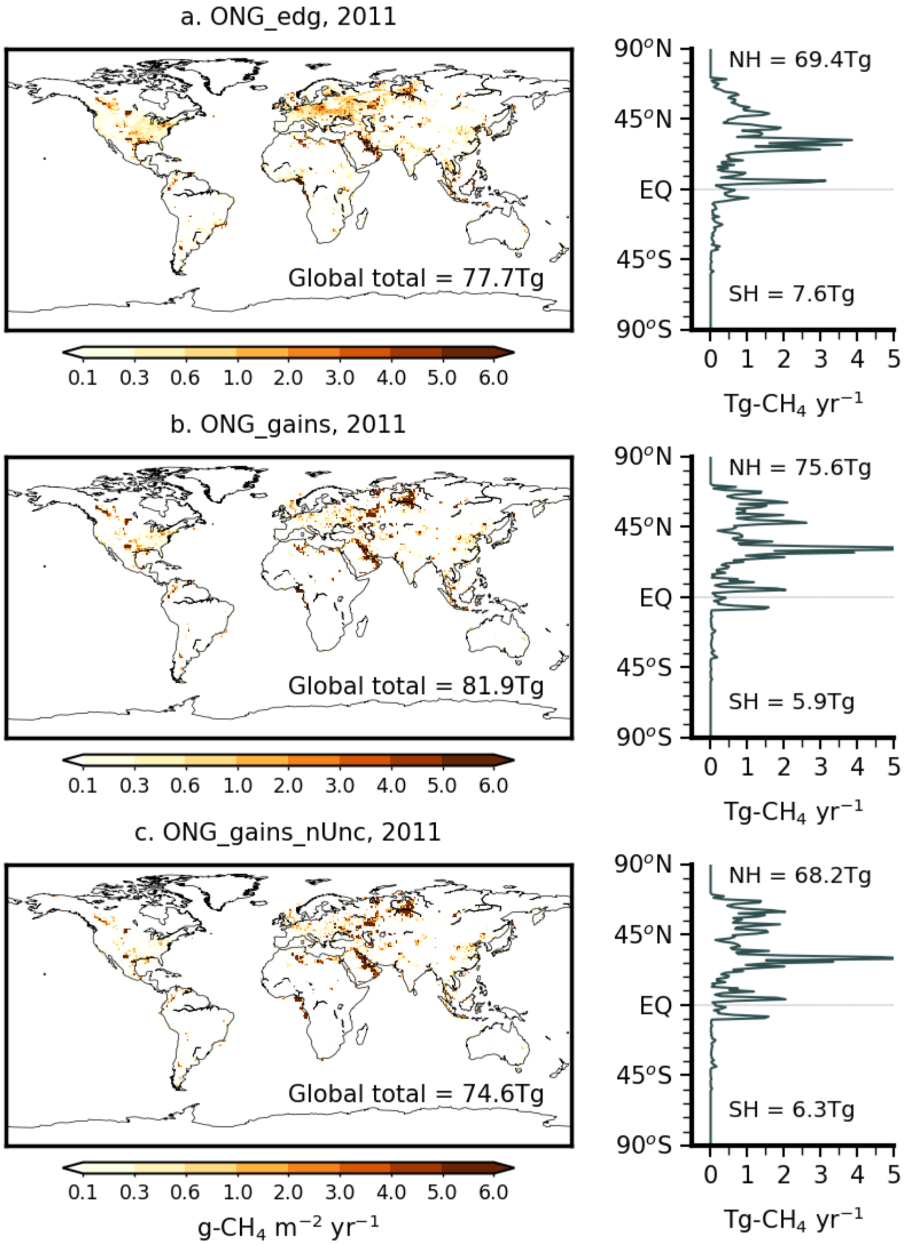

Fig. S16. Spatial and latitudinal distribution of ONG emissions using (a) EDGARv6, (b) GAINSv4, (c) and GAINSv4 without unconventional emissions (c). The GAINS emissions are high in the northern High latitudes.

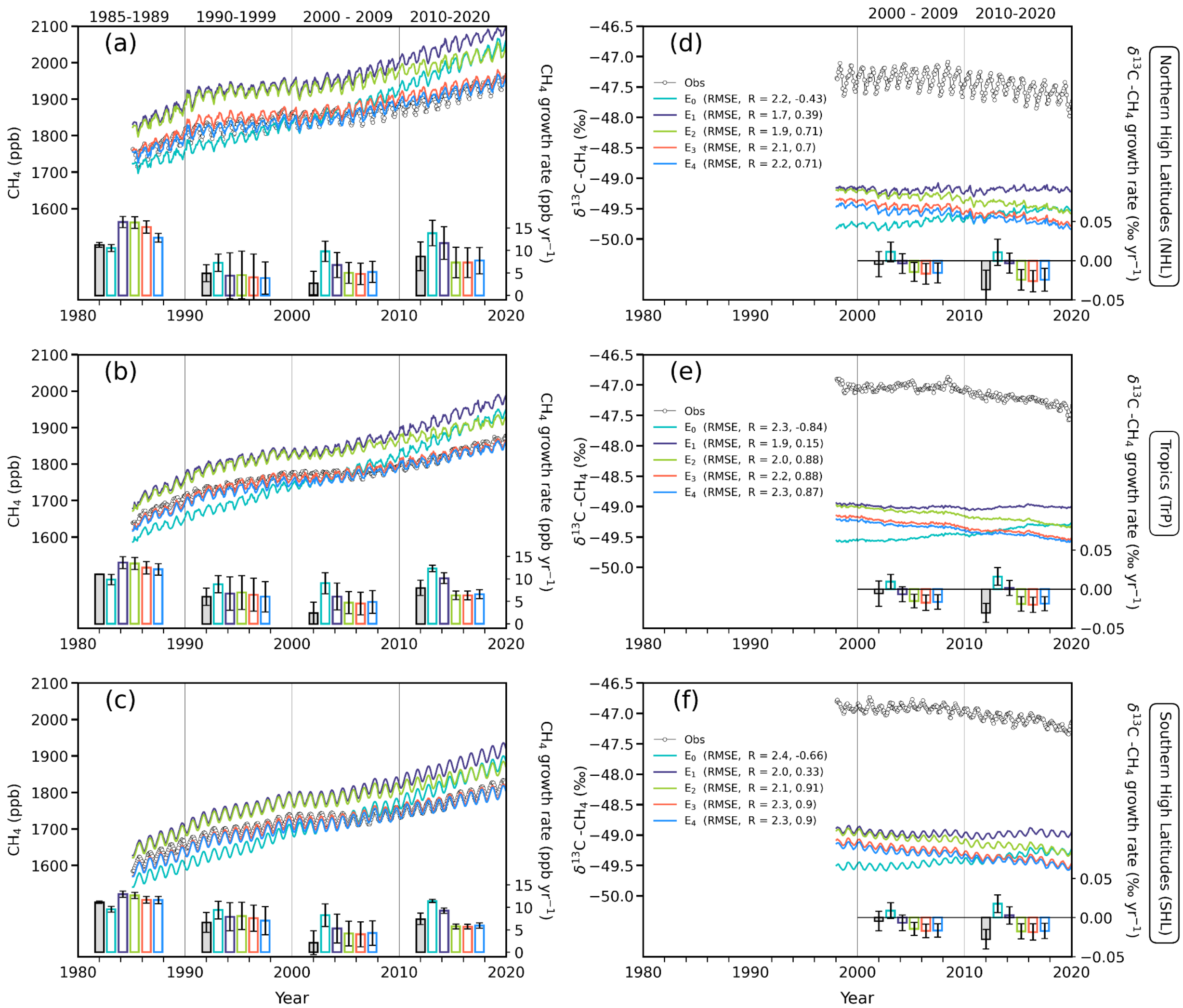

Fig. S17. Same as Fig.2 in the main text, but including all the emission sensitivity simulations.

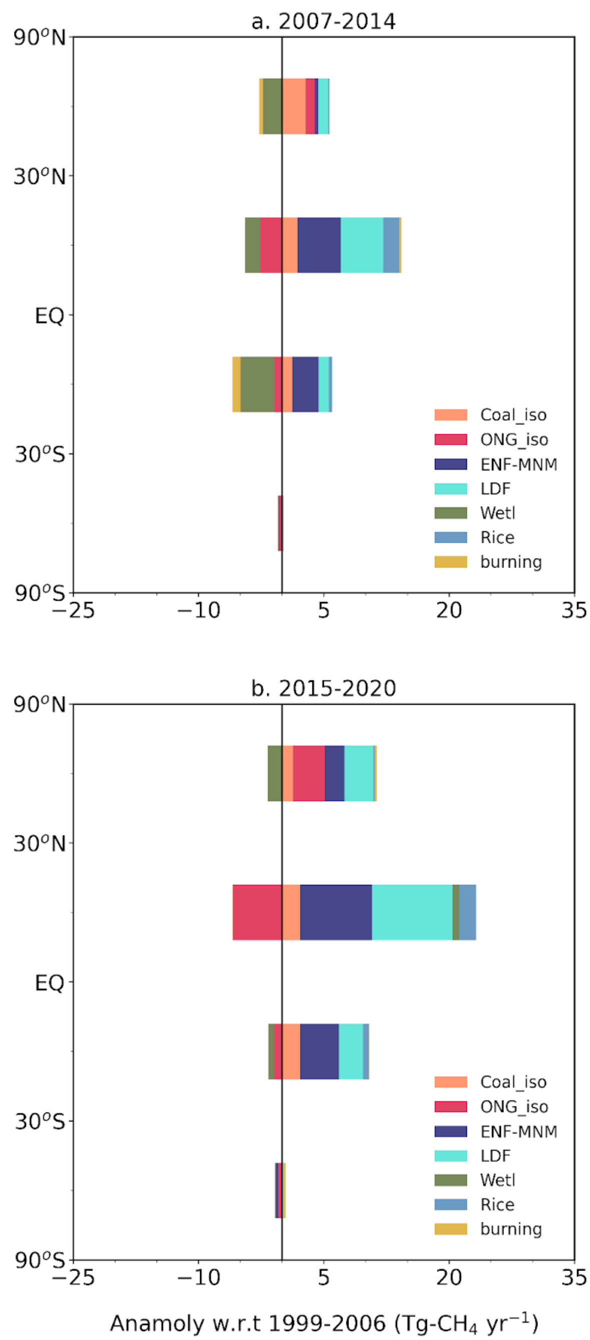

Fig. S18. Change in CH_4 emissions (based on the most plausible E_3 scenario) from individual sectors with respect to 1999-2006 for two different periods at distinct latitude bands.

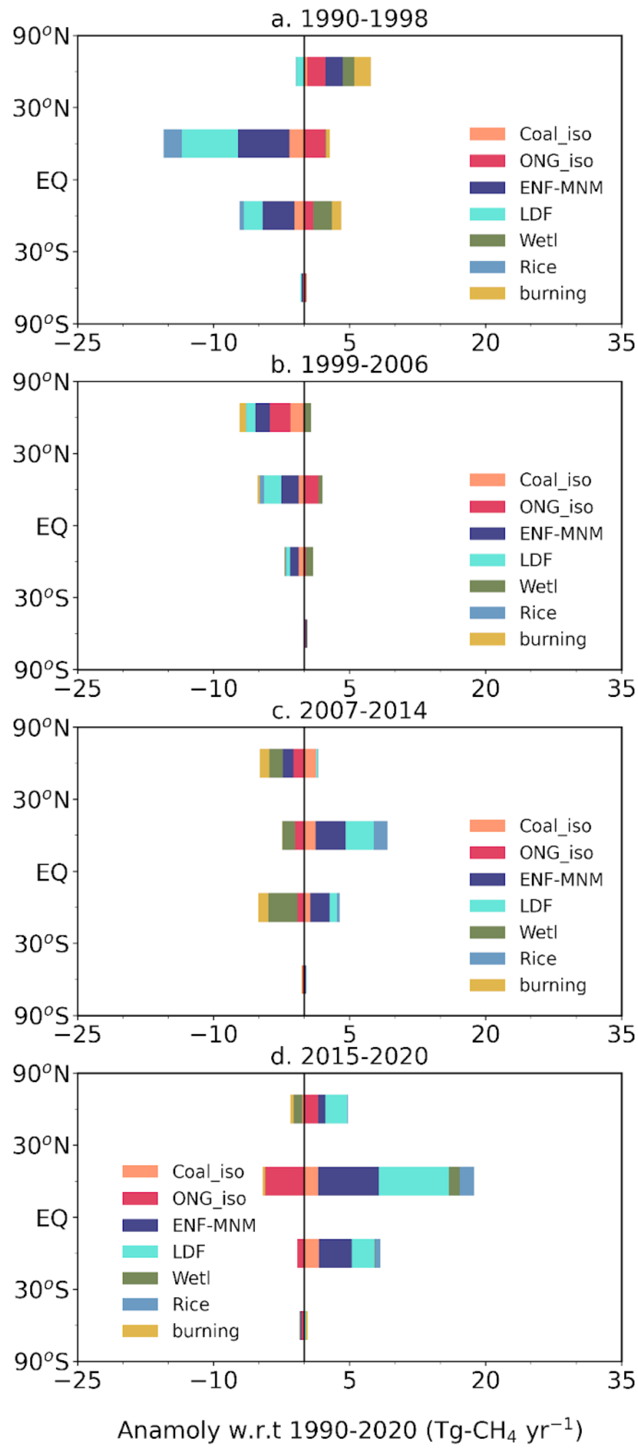

Fig. S19. Change in CH_4 emissions (based on the most plausible E_3 scenario) from individual sectors with respect to 1990-2020 at distinct latitude bands.

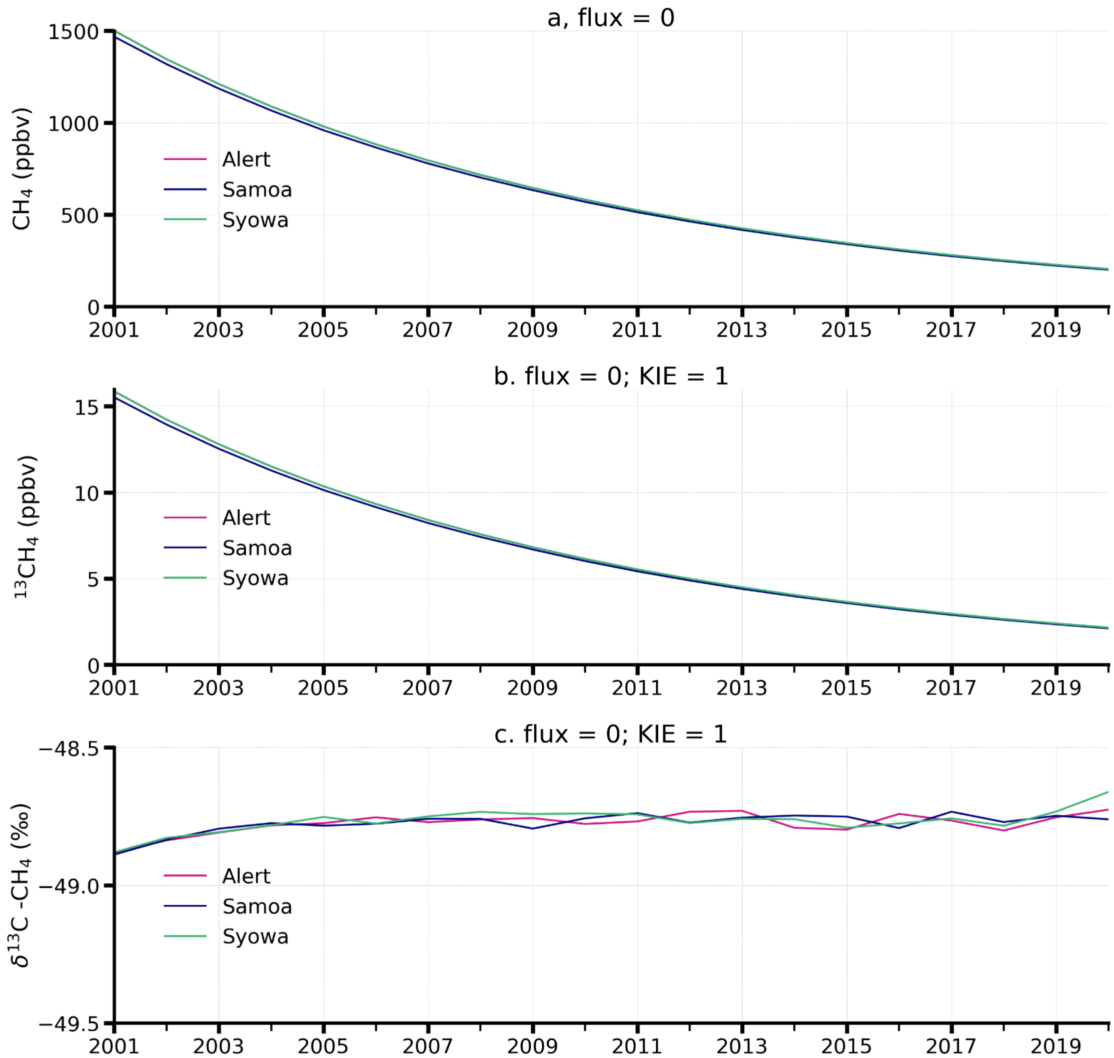

Fig. S20. Checking the tracer mass conservation capability of MIROC4-ACTM in simulating δ^{13}C-CH_4. To assess the tracer mass conservation capability of MIROC4-ACTM in simulating δ^{13}C-CH_4, we conducted a test by disabling fractionation (KIE=1) and emissions (flux = 0) starting from January 1, 2000. The simulations were run for 21 years (2000-2020). Notably, consistent δ^{13}C-CH_4 values across different sites (shown in panel "c") after disabling sink fractionation and emissions indicate that the drift in tracer mass is negligible when simulating δ^{13}C-CH_4 in MIROC4-ACTM for trend analysis purposes.

Table S1: Sources and sinks of CH_4 for 1972-2020, and associated isotopic ratios and kinetic isotope effects (KIE) as used for the simulations of atmospheric $\delta^{13}C$-CH_4, and δD-CH_4 in the base scenario (E_0). For the baseline simulations, we used the global mean source signatures. The KIEs values for the respective sink processes are given at temperature T=296K. Temperature dependencies of the KIEs are accounted for in the model simulations. The mean global total and ±1σ standard deviations are given for 1985-2020 for the baseline simulations. The numbers in red color inside the bracket for fugitive fossil fuel sectors are the most likely emissions from this study.

Source	**Subcategory**	**Data source**	**Global total ($TgCH_4$ yr^{-1}) (1985-2020) (most likely)**	**$\delta^{13}C$-CH_4 (‰)**	**δD-CH_4 (‰)**	**Time/Spatial resolution**
Fossil Fuel (FF)	Coal	EDGARv6 ; revised*	30±6 (27±3)	-35 [a, b]	-232[c]	Monthly, IAV / 0.1x0.1°
	Oil and gas (ONG)		70±11 (80±6)	-44.0 [b, c]	-194[c]	
	Geological	Etiope et al. 2019	37.9 (19)	-49.4[d]	-200[b]	Annual, Cyclostationary/1x1°
Biomass and biofuel burning (BB)	Biomass burning	GFEDv4.0 + AWB + GISS + RCO	34±4	-26.2[c]	-211[c]	Monthly, IAV/1x1°
Microbial	Wetlands	VISIT	162±6	-61.3[e]	-322[c]	Monthly, IAV / 0.5°x0.5°
	Rice		34±3	-62.2[c]	-323[c]	
	ENF & MNM	EDGARv6	109±8	-65.4[c]	-316[c]	Monthly, IAV / 0.1x0.1°
	Waste dump & Landfills		66±9	-55.0[a]	-298[c]	

	Termites	GCP, 2020	17	-63.4[c]	-343[c]	Annual, Cyclostationary/ 1x1°
Ocean		Weber et al. [9]	14	-59[a]	-220[b]	Monthly, Cyclostationary
Loss fields and their Kinetic Isotope Effects (KIE) used in forward simulations of atmospheric ^{13}C-CH_4 (KIE^C)and D-CH_4 (KIE^D). The control ^{13}C-CH_4 simulations (shown in Fig. 2) are based on the average KIE^C value for OH (KIE^C_{OH} : (1.0054[f] + 1.0039[g])/2 = 1.00465) from two different studies[f,g] (same as done in Fujita et al. [10]). Individual KIEs are further used for sensitivity analysis (Fig. 4).						
Reactions		Data source		KIE^C	KIE^D	Time resolutions
CH_4 + OH		Spivakovsky et al. [11]; Patra et al. [12],		1.00465	1.286[l]	Monthly, Cyclostationary
CH_4 + Cl		Takigawa et al. [2]		1.066[h]	1.520[h]	Monthly, Cyclostationary
CH_4 + O (1D)		Takigawa et al. [2]		1.013[g]	1.06[g]	Monthly, Cyclostationart
Soil Oxidation		VISIT [13]		1.0201[i]	1.083[i]	Monthly

*We revised a hotspot emission from Prudhoe Bay, Alaska, for the period 1971-2010 based on the model-observation comparison (Fig. S3, details in Supplementary text).

[a]Monteil et al. [14]. [b]Whiticar et al. [15]. [c]Sherwood et al. [16]. [d]Etiope et al. [8]. [e]Oh et al. [17]. [f]Cantrell et al. [4]. [g]Saueressig et al. [5]. [h]Saueressig et al. [18]. [i]Snover & Quay [19]. [l]Gierczak et al. [20].

Table S2. Sensitivity scenarios (shown in Fig. S14), in addition to scenarios discussed in main Table 1. We have shown only those sectors, which are mainly changed for different scenarios. The source signatures are in per mil (‰)

	Coal	ONG	Geological	Wetland	ENF & MNM	Biomass Burning
E_3_const	-35	-44	-49.4	-61.3	-65.4	-26.2
Scoal	-44.6					
Mcoal	Map					
Mong		Map				
Mwetl				Map		
Menf					Map	
Mbb						Map
M_3	Map			Map		Map
M5_Hgeol	Map	Map	-40	Map	Map	Map
M4_Hgeol-og	Map	-40	-40	Map	Map	Map
M3s_Hgeol-og_Scoal	-44.6	-40	-40	Map	Map	Map
M3_Hgeol	Coal		-40	Coal		Coal

References

1. Rice, A. L. *et al.* Atmospheric methane isotopic record favors fossil sources flat in 1980s and 1990s with recent increase. *Proc. Natl. Acad. Sci.* **113**, 10791–10796 (2016).
2. Takigawa, M., Takahashi, M. & Akiyoshi, H. Simulation of ozone and other chemical species using a Center for Climate System Research/National Institute for Environmental Studies atmospheric GCM with coupled stratospheric chemistry. *J. Geophys. Res. Atmospheres* **104**, 14003–14018 (1999).
3. Wang, X. *et al.* The role of chlorine in global tropospheric chemistry. *Atmospheric Chem. Phys.* **19**, 3981–4003 (2019).
4. Cantrell, C. A. *et al.* Carbon kinetic isotope effect in the oxidation of methane by the hydroxyl radical. *J. Geophys. Res. Atmospheres* **95**, 22455–22462 (1990).
5. Saueressig, G. *et al.* Carbon 13 and D kinetic isotope effects in the reactions of CH4 with O(1 D) and OH: New laboratory measurements and their implications for the isotopic composition of stratospheric methane. *J. Geophys. Res. Atmospheres* **106**, 23127–23138 (2001).
6. Sherwood, O. A., Schwietzke, S. & Lan, X. Global δ13C-CH4 source signature inventory 2020. https://doi.org/10.15138/qn55-e011.
7. Ganesan, A. L. *et al.* Spatially Resolved Isotopic Source Signatures of Wetland Methane Emissions. *Geophys. Res. Lett.* **45**, 3737–3745 (2018).
8. Etiope, G., Ciotoli, G., Schwietzke, S. & Schoell, M. Gridded maps of geological methane emissions and their isotopic signature. *Earth Syst. Sci. Data* **11**, 1–22 (2019).
9. Weber, T., Wiseman, N. A. & Kock, A. Global ocean methane emissions dominated by shallow coastal waters. *Nat. Commun.* **10**, 4584 (2019).
10. Fujita, R. *et al.* Global and Regional CH4 Emissions for 1995–2013 Derived From Atmospheric CH4, δ13C-CH4, and δD-CH4 Observations and a Chemical Transport Model. *J. Geophys. Res. Atmospheres* **125**, e2020JD032903 (2020).
11. Spivakovsky, C. M. *et al.* Three-dimensional climatological distribution of tropospheric OH: Update and evaluation. *J. Geophys. Res. Atmospheres* **105**, 8931–8980 (2000).
12. Patra, P. K. *et al.* Observational evidence for interhemispheric hydroxyl-radical parity. *Nature* **513**, 219–223 (2014).
13. Ito, A., Patra, P. K. & Umezawa, T. Bottom-Up Evaluation of the Methane Budget in Asia and Its Subregions. *Glob. Biogeochem. Cycles* **37**, e2023GB007723 (2023).

14. Monteil, G. *et al.* Interpreting methane variations in the past two decades using measurements of CH_4 mixing ratio and isotopic composition. *Atmospheric Chem. Phys.* **11**, 9141–9153 (2011).

15. Whiticar, M. & Schaefer, H. Constraining past global tropospheric methane budgets with carbon and hydrogen isotope ratios in ice. *Philos. Trans. R. Soc. Math. Phys. Eng. Sci.* **365**, 1793–1828 (2007).

16. Sherwood, O. A., Schwietzke, S., Arling, V. A. & Etiope, G. Global Inventory of Gas Geochemistry Data from Fossil Fuel, Microbial and Burning Sources, version 2017. *Earth Syst. Sci. Data* **9**, 639–656 (2017).

17. Oh, Y. *et al.* Improved global wetland carbon isotopic signatures support post-2006 microbial methane emission increase. *Commun. Earth Environ.* **3**, 1–12 (2022).

18. Saueressig, G., Bergamaschi, P., Crowley, J. N., Fischer, H. & Harris, G. W. Carbon kinetic isotope effect in the reaction of CH4 with Cl atoms. *Geophys. Res. Lett.* **22**, 1225–1228 (1995).

19. Snover, A. K. & Quay, P. D. Hydrogen and carbon kinetic isotope effects during soil uptake of atmospheric methane. *Glob. Biogeochem. Cycles* **14**, 25–39 (2000).

20. Gierczak, T., Talukdar, R. K., Herndon, S. C., Vaghjiani, G. L. & Ravishankara, A. R. Rate Coefficients for the Reactions of Hydroxyl Radicals with Methane and Deuterated Methanes. *J. Phys. Chem. A* **101**, 3125–3134 (1997).